International Communications in Heat and Mass Transfer 152 (2024) 107272

Contents lists available at ScienceDirect

International Communications in Heat and Mass Transfer

journal homepage: www.elsevier.com/locate/ichmt

Direct numerical simulation of pathogen-laden aerosol dispersion in buoyancy-driven turbulent flow within confined spaces

Akim Lavrinenko *, Alexandre Fabregat, Fernando Gisbert, Jordi Pallares

Department of Mechanical Engineering, Universitat Rovira i Virgili, Av. Països Catalans 26, 43007 Tarragona, Spain

ARTICLE INFO

PACS:
44.35
c 44.25
f 47.27

Keywords:
Particle transport
Airborne infectious diseases
Mixing rate
Natural convection
Turbulent dispersion
Differentially heated cavity

ABSTRACT

Turbulent dispersion of particles is vital in understanding the transmission of airborne infectious diseases. Transmission primarily occurs via inhalation of pathogen-laden aerosols released when infected individuals breathe, talk, cough, or sneeze. We employ Direct Numerical Simulations to investigate aerosol dispersion in an idealized cubic room subjected to high Rayleigh numbers induced by natural convection. Temperature difference on opposing walls drive turbulent flow with a dominant large-scale recirculation. The initial aerosol distribution consists of spherical solid particles (0.1–2.5 μm in diameter) randomly seeded within a spheres initially located on the main diagonal of the cavity. Analysis of particle relative dispersion and concentration variance reveals strong inhomogeneity, highlighting lower dispersion in the central area of the room and significantly higher dispersion near the walls. Additionally, we introduce a new analytical model for aerosol cloud dispersion within the cubic room, comparing it with Direct Numerical Simulations. Results suggest that closed-form models in some cases provide reasonable estimates of particle mixing time. According to simulation results, homogeneous mixing inside the room is attained 500 s after the release even for the most unfavorable conditions. This research advances our comprehension of indoor aerosol dispersion, a critical factor for evaluating the risks associated with airborne disease transmission.

E-2000 MSC

76F25
76T15

1. Introduction

The transport of aerosols in turbulent flows plays a central role in various processes. Its practical applications span various fields, including environmental and climate studies, human health and safety, industrial processes, and fundamental fluid dynamics research.

In industrial applications, such understanding aids the optimization of processes like combustion, spray coating, and powder handling [1–3]. The behavior of particles in turbulent conditions also affects the transport and distribution of aerosols, influencing climate and weather patterns by interacting with sunlight, radiation balance, and cloud formation [4]. It is instrumental in gauging and reducing environmental impact, as seen in the dispersion of pollutants in the atmosphere and aquatic systems [5–7]. These studies [8–10] deepens our understanding of fluid flow behavior, mixing processes, and the interplay between dispersed and carrier phases.

Also, comprehending how aerosols travel in turbulent environments is essential in grasping the spread of airborne infectious diseases. This includes diseases such as the common cold, influenza, chickenpox, measles, tuberculosis [11], and more recently, COVID-19 [12]. By July 2023, the latter has sadly resulted in over 691 million cases and exceeded 6.9 million fatalities worldwide [13]. These insights into aerosol transport mechanisms hence hold significant implications for public health. Centers for Disease Control [14] and Prevention and the World Health Organization [15] urges to accelerate the research and development process, and develop new rules and standards to mitigate the spread of diseases transmitted by pathogen-laden aerosols.

The COVID-19 pandemic has underscored the importance of gaining a deeper understanding of physics of pathogen-laden transport. Research on this subject has been ongoing for a considerable period of time and various methods have been employed [16–21]. Piscitelli et al. [22] discusses key aspects relevant to the airborne disease transmission in indoor settings where SARS-CoV-2 can readily spread, persist, and

* Corresponding author.
E-mail addresses: akim.lavrinenko@urv.cat (A. Lavrinenko), alexandre.fabregat@urv.cat (A. Fabregat), fernando.gisbert@urv.cat (F. Gisbert), jordi.pallares@urv.cat (J. Pallares).

https://doi.org/10.1016/j.icheatmasstransfer.2024.107272

Available online 1 February 2024

infect others, particularly in the presence of asymptomatic or mildly symptomatic individuals who are already infected. Nazaroff [23] concludes that transmission predominantly occurs indoors, through the inhalation of airborne particles, up to 50 μm in diameter. Lima et al. [24] review the dispersion characteristics of SARS-CoV-2 virus in indoor air through using the results of ten selected studies, revealing key factors such as particle size, viral load, and distance traveled, and finding inconclusive evidence regarding the impact of air temperature and relative humidity on aerosol dispersion. Ciuzas et al. [25] explored indoor air quality, providing insights into the dynamic patterns of indoor particulate matter across different pollution episodes. In a recent analysis of literature concerning airborne transmission and indoor air quality, conducted by Hobeika [26], authors raise concern about vulnerabilities in indoor air quality and ventilation strategies. The study underscores the imperative for regulatory measures in buildings to address air quality and ventilation, particularly in light of the knowledge surrounding the transmission of virus-laden particles through the air. Wei and Yuguo [27] critically reviewed the literature on the airborne spread of infectious diseases within indoor environments and proposed strategies for infection control at various stages of transmission. The numerical study conducted by Dbouk and Drikakis [28] investigates particle transport within a simplified room with natural ventilation. The study concludes that allowing inhabitants to vacate the space for a sufficient period of time facilitates the complete evacuation of residual aerosol particles, thus mitigating potential indoor air hazards. Gao and Niu [29] use Computational Fluid Dynamics (CFD) with a drift-flux and semi-empirical deposition models, to predict the spatial distribution of particle concentration and study the effect of different particles sizes on human exposure to the particulate matter.

Coughing and sneezing, characterized as violent expiratory events, stand out as one of the primary sources of virus-laden aerosols responsible for disease transmission. Direct Numerical Simulations (DNS) by Fabregat et al. [30,31] showed that human violent expiratory events, could be divided into two stages. In the first stage that starts immediately after the violent expiratory event, the turbulent particle dispersion is dominated by the jet/puff flow generated by the rapid exhalation. Studies suggest that the aerosol clouds, at the culmination of the first stage of exhalation, can be roughly estimated as a sphere with a radius of about 0.3 m [32,33]. A second stage starts approximately 2 s after exhalation, once significant fraction of the turbulent kinetic energy has already dissipated due to viscosity. The primary drivers of particle dispersion then become ambient air currents influenced by natural factors, such as room temperature gradients, or forced convection mechanisms like Heating, Ventilation, and Air Conditioning systems [34]. Consequently, the long-term distribution and mixing attributes of the particles mostly depend on these large-scale ambient flows. To improve our understanding of inhomogeneous turbulent flow and aerosol dispersion, we numerically investigate here the mixing properties of an idealized particle cloud resembling that genereated by a rapid exhalation in a cubical room with no ventilation using fully-resolved simulations. Building upon the existing research [30,31], this study focuses on the second stage of violent expiratory event, when the dispersion of pathogen-laden particle clouds is governed by a large-scale buoyancy-driven flow. Through DNS with Lagrangian Particle Tracking (LPT), we model the airflow and pathogen-laden particles within a cubical room with sides of ~ 3 m subjected to a temperature difference of 1.24 K applied to two pairs of differentially heated opposed walls. By analyzing the trajectories of the particles within the cloud, we examine the spatial dependence of the mixing time for the particle cloud and given particle size. Using particle relative dispersion, we compare the mixing time of the particle cloud in our study with established regimes. This allows us to assess the behavior of the particle cloud in terms of dispersion characteristics. Additionally, utilizing the temporal evolution of the particle relative dispersion, we calculate the dispersion coefficient, which provides quantitative information about the spreading and diffusion of particle cloud within the room. The costly DNS results are evaluated against closed-form models to appraise their predictive capabilities regarding mixing rates under idealized flow conditions. Two distinctive models are assessed - first, novel Gaussian model derived from an instantaneous aerosol point source, and second, a semi-analytical model for the dispersion of a continuous source proposed by Lau et al. [35]. The mixing times calculated using these closed models are compared to those from the DNS using the particle concentration variance as a comparative measure.

Mathematical and physical models are presented in Section 2. Simulation results, including instantaneous snapshots of the thermal flow, averaged outcomes, temporal particle relative dispersion and variance of the particle concentration, and a comparison with analytical model predictions, are presented and discussed in Section 3, 4. Conclusions drawn from the findings are outlined in Section 5. Additional details regarding the LPT model can be found in Appendix A (Section 6), while Appendix B (Section 7) provides, for completness, the derivation of the dispersion model equation proposed by Lau et al. [35].

2. Mathematical methods

In this study, we use the identical numerical setup described in Lavrinenko et al. [36]. The computational domain, representing an idealized cubical room, consists in a cavity of side length $l_s = 3.148$ m filled with air at average temperature $T_0 = 300$ K (see Fig. 1).

The bottom horizontal (floor) and the left vertical wall are kept at a constant temperature $T_h = T_0 + \Delta T/2$ while the top horizontal (ceiling) and the opposite right vertical wall which are kept at $T_c = T_0 - \Delta T/2$. The remaining vertical walls, normal to z, are assumed adiabatic. Temperature difference ΔT is 1.243 K and gravity acts in the $-y$ direction.

The pathogen-laden aerosol cloud, representing a human violent exhalation at the second stage, is modelled by randomly seeding smooth solid spherical particles within spheres with a radius of 0.3 m. We consider the dispersion of a total of 25 particle clouds (i.e. 5 locations of the clouds and 5 particle sizes). The trajectories of each cloud are tracked throughout the entire simulation period, which corresponds to 1.4×10^3 s (23 min). Using the particle trajectories of each cloud, we compare the mixing by utilizing the particle relative dispersion and the variance of the particle concentration.

Fig. 2 illustrates the initial locations of the particle clouds considered in this study. The figure displays the 5 clouds located along the main diagonal of the cavity. Each cloud comprises 5 particle sizes: 0.1, 0.5, 0.7, 1.3, and 2.5 μm. On average, there are 230 particles of each size

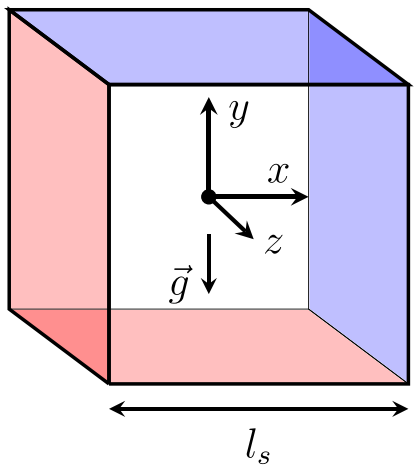

Fig. 1. Sketch of the computational domain consisting of a $\left[-\frac{1}{2},\frac{1}{2}\right]^3$ in non-dimensional units. Red and blue surfaces represent hot and cold walls respectively. (For interpretation of the references to color in this figure legend, the reader is referred to the web version of this article.)

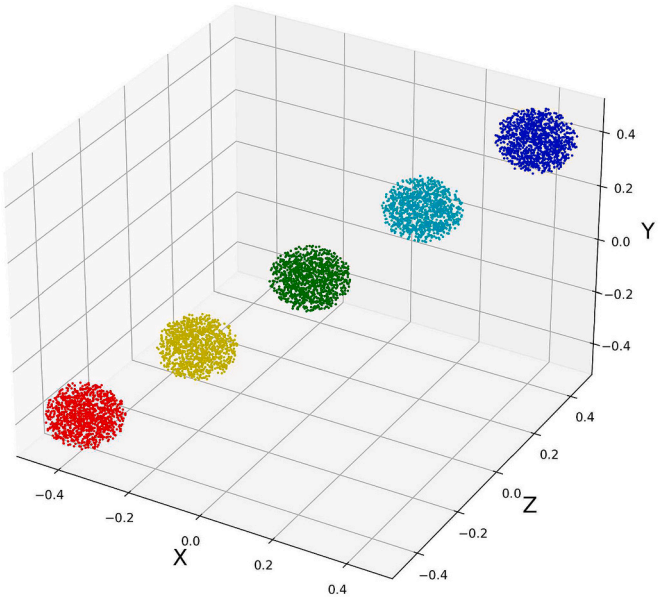

Fig. 2. Initial position of the clouds (Table 1 provides the center coordinates of each cloud).

present in each cloud. Table 1 provides the spatial coordinates of the considered cloud center locations along with their corresponding colors.

2.1. Carrier phase model

Assuming incompressibility conditions, the non-dimensional mass, momentum and thermal energy conservation equations under the Boussinesq approximation can be written as:

$$\frac{\partial u_i}{\partial x_i} = 0 \tag{1}$$

$$\frac{\partial u_i}{\partial t} + u_j\frac{\partial u_i}{\partial x_j} = -\frac{\partial p}{\partial x_i} + \frac{Pr}{\sqrt{Ra}}\frac{\partial^2 u_i}{\partial x_j \partial x_j} + Pr\theta\delta_{i2} \tag{2}$$

$$\frac{\partial \theta}{\partial t} + u_j\frac{\partial \theta}{\partial x_j} = \frac{1}{\sqrt{Ra}}\frac{\partial^2 \theta}{\partial x_j \partial x_j} \tag{3}$$

where t is time, u_i is the velocity component in the direction x_i, p is pressure and $\theta = \frac{T-T_0}{\Delta T}$ is the temperature fluctuation. The Rayleigh and Prandtl number are defined as $Ra = \left(g\beta\Delta T l_s^3\right)\Big/(\nu\alpha) = 3.6 \times 10^9$ and $Pr = \nu/\alpha = 0.7$ respectively where the velocity, length, time and temperature scales are $u_s = \alpha\sqrt{Ra}/l_s = 0.427$ m s^{-1}, $l_s = \alpha\sqrt{Ra}/u_s = 3.148$ m, $t_s = l_s/u_s = 7.372$ s and $T_s = \Delta T = 1.243$ K respectively.

Eqs. (1)–(3) are solved using NEK5000 [37], an open-source, high-order spectral element method (SEM) based solver designed for solving the incompressible Navier–Stokes equations. NEK5000 utilizes Nth-order tensor-product Lagrange polynomials as basis functions on the Gauss–Lobatto–Legendre quadrature points within each element, ensuring efficient evaluation and low storage costs for operators [38].

The solver employs a semi-implicit kth-order Backward Difference Formula (BDFk) and kth-order Extrapolation (EXTk) timestepping method. The time derivative is approximated using BDFk, while the nonlinear terms and other forcings are handled with EXTk. Viscous and pressure terms are treated implicitly, leading to the solution of a linear unsteady Stokes problem at each time step. This problem involves Helmholtz equations for each component of velocity, temperature, or scalars, and a Poisson equation for pressure [39]. NEK5000 is a widely utilized tool for both DNS and LES simulations across various flow configurations and applications [40–42].

The computational grid, with a total of approximately 300 million nodes, ensuring explicit resolution of all spatial and temporal scales as per the resolution criteria proposed by Scheel et al. [43] for similar buoyancy-driven flow configurations. The maximum and minimum grid cells are $\Delta X_{max} = \Delta Y_{max} = \Delta Z_{max} = 3.3 \times 10^{-3}$ and $\Delta X_{min} = \Delta Y_{min} = \Delta Z_{min} = 1.4 \times 10^{-4}$ non-dimensional units, respectively. For further details on the numerics and mesh generation, please refer to Fabregat and Pallares [44].

The Spectral Element Method (SEM) spatial discretization used in NEK5000 where the numerical approximation in each element can be expressed as a three-dimensional Legendre polynomial expansion of order N^3 is used to interpolate the particle velocity on the previous time step or in any other intermediate time in the predictor-corrector approach used in Exponential-Lagrangian Tracking Schemes (see details in [44]).

Table 1
Particle cloud centroid coordinates and size-averaged dispersion coefficient of each sphere.

No	Color	$x,y,z,$	$\langle K_{sa}\rangle$ m^2 s^{-1}
1	red	−0.4, −0.4, −0,4	0.0133
2	yellow	−0.2, −0.2, −0,2	0.0088
3	green	0.0, 0.0, 0.0	0.0047
4	cyan	0.2, 0.2, 0,2	0.0129
5	blue	0.4, 0.4, 0,4	0.0110
		mean	0.01

2.2. Discrete phase model

Particles are modelled as idealized globular and smooth spheres. Given the small particle size and high dilution, we assume a one-way coupling between the phases and neglect the particle collisions. When a particle deposits on the wall, it is subsequently reseeded to a random location within the domain.

The position of a given particle x_i^* can be written as:

$$\frac{dx_i^*}{dt} = u_i^* \tag{4}$$

where the particle velocity u_i^* can be determined as:

$$\frac{du_i^*}{dt} = \underbrace{\frac{u_i - u_i^*}{St_p}}_{\text{Drag}} + \underbrace{n_g\delta_{i2}}_{\text{Buoyancy}} + \underbrace{n_{th}\frac{\partial T}{\partial x_i}}_{\text{Thermophoresis}} + \underbrace{n_l\varepsilon_{ijk}\left[u_j^* - u_j\right]\omega_k}_{\text{Lift}} + \underbrace{n_i(t)}_{\text{Brownian}} \tag{5}$$

where St_p is the particle Stokes number, n_g is the magnitude of the buoyancy force experienced by a particle, δ_{ij} is the Kronecker delta, n_{th} is the pre-factor of the non-dimensional temperature gradient, n_l is the lift proportionality factor, ε_{ijk} is the Levi-Civita symbol, $\vec{\omega} = \overrightarrow{\nabla} \times \vec{u}$ is the flow vorticity and n_i is the Brownian force.

The particle transport model presented in Eqs. (4)–(5) assumes that there are five relevant forces acting on the particle, namely, hydrodynamic drag and lift, buoyancy, thermophoresis and Brownian. The definitions of the different parameters in Eq. (5) can be found in Appendix A (Section 6) of this paper.

2.3. The Gaussian dispersion model for an instantaneous point source

Computational Fluid Dynamics (CFD) simulations, such as Direct Numerical Simulations (DNS) and Large Eddy Simulations (LES), are widely used for investigating particle dispersion and are valuable for research and validation purposes. However, conducting these simulations demands substantial computational resources and generates vast data sets that necessitate time-consuming post-processing for the clear results and thus decision-making. As a result, there is a critical need for a reliable and efficient engineering tool capable of accurately estimating

aerosol concentrations in indoor environments.

There, we develop a Gaussian dispersion model that assumes an instantaneous injection of aerosols from a point source, with source strength S. Particle cloud advection is considered along the path of the large-scale recirculation generated by the thermally active walls (see Fig. 3a). The cloud is assumed to be transported with a constant velocity (u_c) and dispersed by a constant turbulent diffusion coefficient (K). The distribution of particles along the path parallel to the four walls of the cavity of the large-scale recirculation is modelled similarly to the dispersion along a straight three-dimensional square duct sketched in Fig. 3b. In Fig. 3a arrows from 1 to 4 show the dominant circulation. Particle cloud advection parallel to the four walls of the cavity is modelled as particle cloud transport in a square duct sketched in Fig. 3b. Each cube comprising the duct (from 1 to 4) accounts for the transport under the transformed system of coordinates of the cavity shown in Fig. 3a. In order to model the recirculating flow within the cavity, we transform the system of the coordinate of cubes 2–4 (Fig. 3b). In case of cube 2, the system if coordinates is rotated 90°, for cube 3, 180° and for cube 4, 270 the transformed coordinate system of the domain, shown in Fig. 3b, has ξ, η and z as the streamwise, vertical and horizontal directions respectively. The domain has a height and width of l_s and a streamwise dimension of $4l_s$, which corresponds, approximately to the path length of the large-scale recirculation sketched with four arrows in Fig. 3a.

The dispersion of an instantaneous point source in an unbounded domain can be written as (see for example Seinfeld and Pandis [45] and Drivas et al. [46]).

$$c(x,y,z,t) = \frac{S}{8(\pi t K)^{3/2}} exp\left[-\frac{\left(x+\frac{l_s}{2}-x_0+u_c t\right)^2}{4Kt} - \frac{\left(y+\frac{l_s}{2}-y_0\right)^2}{4Kt} - \frac{\left(z+\frac{l_s}{2}-z_0\right)^2}{4Kt} \right] \quad (6)$$

where c is concentration ($particles/m^3$), S is source strength ($particles/s$), K is dispersion coefficient ($m^2\ s^{-1}$), t is time (s) and u_c is velocity ($m\ s^{-1}$).

Eq. (6) can be adopted to the present simulation by expressing the original system of coordinate (x,y,z) in Fig. 3a to the transformed system of reference (ξ,η,z) shown in Fig. 3b. An instantaneous source is initially located at position ξ_0, η_0, z_0 inside the room with a constant streamwise velocity u_c. The new expression now reads:

$$c(\xi,\eta,z,t) = \frac{S}{8(\pi t K)^{3/2}} exp\left(-\frac{\left(\xi+\frac{l_s}{2}-\xi_0-u_c t\right)^2}{4Kt} \right) R_z R_\eta \quad (7)$$

where ξ_0, η_0 and z_0 ($-\ l_s/2 < \xi_0 < l_s/2$, $-\ l_s/2 < \eta < l_s/2$, $-\ l_s/2 < z < l_s/2$) are the coordinates of the point source emission. The sum in the term R_z accounts for the particle reflection on front and back walls of the channel located $z = -\ l_s/2$, $z = l_s/2$ and R_η accounts for the particle reflection on the bottom and top walls located at $\eta = -l_s/2$ and $\eta = l_s/2$ respectively.

The dispersion and reflection terms along the z direction:

$$R_z = \sum_{i=-\infty}^{i=\infty} \left[exp\left(-\frac{\left(z+\frac{l_s}{2}+2il_s-z_0\right)^2}{4Kt} \right) + exp\left(-\frac{\left(z+\frac{l_s}{2}+2il_s+z_0\right)^2}{4Kt} \right) \right] \quad (8)$$

Correspondingly along the η direction,

$$R_\eta = \sum_{i=-\infty}^{i=\infty} \left[exp\left(-\frac{\left(\eta+\frac{l_s}{2}+2il_s-\eta_0\right)^2}{4Kt} \right) + exp\left(-\frac{\left(\eta+\frac{l_s}{2}+2il_s+\eta_0\right)^2}{4Kt} \right) \right] \quad (9)$$

The instantaneous concentration distribution obtained from Eq. (7) in the channel is mapped into the cavity by transforming the system of coordinates ξ,η,z into the system of coordinates x, y, z, with its origin located at the center of the cavity (see Fig. 3a).

2.4. Semi-analytic model by Lau et al. [35]

Lau et al. [35] developed a semi-analytical model to examine the two-dimensional concentration of pathogen-laden particles in indoor

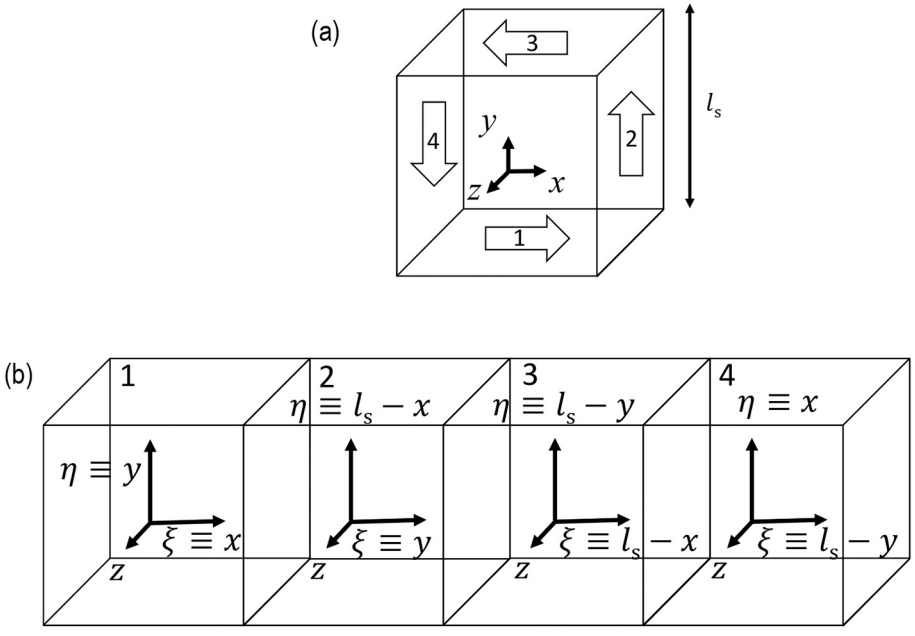

Fig. 3. (a) Sketch of the large-scale flow recirculation. (b) The channel used to model the dispersion process near the bottom wall (1), right vertical wall (2), top wall (3) and left vertical wall (4).

environments. An infectious person is considered as the continuous source of infectious aerosols. All aerosols have the same size and carry the same amount of virus. The aerosols are transported by advection caused by the airflow with velocity u_c, which follows the recirculating loop. It is assumed that the aerosols are passively released into the flow stream, as the expelled air from the mouth and nose during breathing and talking. In the absence of aerosol removal by ventilation, biological deactivation of the virus, and gravitational settling the time evolution of the concentration can be written as:

$$C(x,y,t) = \frac{2R}{4\pi Kh} \int_0^t \sum_{m=-\infty}^{\infty} \left[exp - \frac{\left(x + \frac{l_x}{2} - u_c t - x_0 - 2ml\right)^2}{4Kt} + exp - \frac{\left(x + \frac{l_x}{2} + ut + x_0 - 2ml\right)^2}{4Kt} \right] \cdot \cdot \sum_{n=-\infty}^{\infty} \left[exp - \frac{\left(y + \frac{l_x}{2} - y_0 - 2nw\right)^2}{4Kt} + exp - \frac{\left(y + \frac{l_x}{2} + y_0 - 2nw\right)^2}{4Kt} \right] \mathrm{d}t \tag{10}$$

where C is the concentration of infectious aerosols ($aerosols/m^2$) at all points on the surface of the looping airflow, R is the infectious aerosol emission rate ($aerosols/\mathrm{s}$), l, w, h are length, width and height of the room respectively (m), x_0, y_0 is point source location. For completeness, more details on the original model are given in the Appendix B 7 of this paper and in the original paper of Lau et al. [35].

Eq. (10) represents a model for continuous aerosol source, where the number of particles always increases. In contrast, both in the DNS and the model given in Eq. (7), the particle count remains constant, modeling particle cloud from a single isolated violent respiratory event. To allow direct comparison with the DNS results for a finite release of particles, the model of Lau et al. [35] was modified to consider injection of particles into the domain only during the exhalation event, which lasts for 0.4 s ($t = 0$ to $t = t_{inj} = 0.4$ s). Beyond t_{inj}, the aerosol count is set constant by subtracting additional aerosols every time step from the continuous source, as shown in Eq. (11).

$$C_{cough}(x,y,t) = C(x,y,t) - \left(C(x,y,t) - C_{inj}(x,y,t)\right) \tag{11}$$

Here, C_{cough} is the concentration for times $t > t_{inj}$, C is the concentration calculated using Eq. (10), and C_{inj} is the concentration calculated during the time interval from $t = 0$ to t_{inj}.

2.5. Particle dispersion

In order to quantify the ability of the flow to disperse and homogenize passive particle cloud across the entire room we use the relative dispersion of the particles and the variance of particle concentration.

The squared relative dispersion D^2 is defined as the average square distance over all particles pairs and it can be calculated using [7]:

$$D^2 = \frac{1}{P} \sum_{i,j} \left[x_i^* - x_j^*\right]^2 + \left[y_i^* - y_j^*\right]^2 + \left[z_i^* - z_j^*\right]^2 \tag{12}$$

where x^*, y^*, z^* are the individual particle coordinates, P is the number of all possible particle pairs and n is total number of particles and it is defined as:

$$P = \sum_{k=1}^{n-1} (n-k) = \frac{n(n-1)}{2} \tag{13}$$

Particle dispersion has been historically characterized by means of the average particle pair separation D^2. Several regimes for the evolution of $D^2 \sim t^\nu$ have been investigated. Initially the relative velocity of the particles remains relatively constant, resulting in what is known as standard eddy-diffusion regime characterized by a linear scaling if inter particle distance ($\nu = 1$). At very long times, when particle pair separation is much larger than the integral scale of the flow, the velocity field becomes uncorrelated, and the typical inter-particle distance exhibits square-root scaling in time ($\nu = 2$). Richardson proposed a super diffusive regime ($\nu = 3$) for particle separation within the inertial range of turbulence. Finite Reynolds number effects, flow intermittency and the fact that the particle distance must be between the Kolmogorov and integral length scales make the identification of this regime difficult [47].

For a system with particles homogeneously mixed within a cubical cavity, the theoretical value of relative dispersion is given by $D_c^2 = \frac{l_s^2}{2} = 4.95\ \mathrm{m}^2$, where l_s represents the length of the cavity wall ($l_s = 3.148$m). Similarly, for the spherical shape domain with fully mixed conditions, the theoretical relative dispersion is expressed as $D_s^2 = \frac{3d^2}{10} = 0.027\ \mathrm{m}^2$, where d denotes diameter of the sphere in meters ($d = 0.6$ m).

Initially, particles are homogeneously distributed inside the spheres, thus non-dimensional relative dispersion can be defined as:

$$D^{2^*} = \frac{D^2 - D_s^2}{D_c^2 - D_s^2} \tag{14}$$

where $D^{2^*} \approx 1$ corresponds to homogeneous distribution of particles inside the cubical cavity.

The rate of growth of average square distance over all particles pairs can be related with the relative diffusivity as [48]:

$$K = \frac{1}{2} \frac{dD^2}{dt} \tag{15}$$

The variance of particle concentration serves as a metric for quantifying deviations from a uniform concentration distribution. To implement this approach, we partitioned our cavity into five equal segments in each direction, resulting in a total of N equally sized bins. We then monitored the particle concentration within each bin and compared them to the expected uniform distribution. The variance is defined as [49]:

$$\sigma^2 = \frac{1}{N} \sum_{i=1}^{N} (n_i - \mu)^2 \tag{16}$$

where N is number of the bins, n_i is particle concentration in the bin and μ is the mean particle concentration:

$$\mu = \frac{1}{N} \sum_{i=1}^{N} n_i \tag{17}$$

3. Results and discussion

As an example of the large scale flow structure Fig. 4, shows slices of the non-dimensional temperature field at two different locations. The left panel of the figure shows the temperature contours of the cross-section of the room on the plane $z = 0$ and it depicts the distinct features of the large-scale, persisting, clockwise circulation pattern on the temperature field. Distinct hot air vertices are noticeable close to the left and bottom hot walls, while the top and right cold walls display vigorous mixing of hot and cold air. Within the central region, the temperature field maintains a relatively stable and tranquil state, with only minor fluctuations observed around the average temperature (T_0). The right panel of the figure shows a slice at $y = 0.495$, located within the boundary layer of the top cold wall. This layer is characterized by the presence of cold fluid streaks that align roughly with the dominant flow direction, which is from left to right.

This pattern is characterized by a distinct velocity and temperature profiles. Fig. 5 shows the time-averaged non-dimensional temperature ($\langle T \rangle$) and velocities ($\langle u_x \rangle$, $\langle u_y \rangle$) along the bisector of the vertical

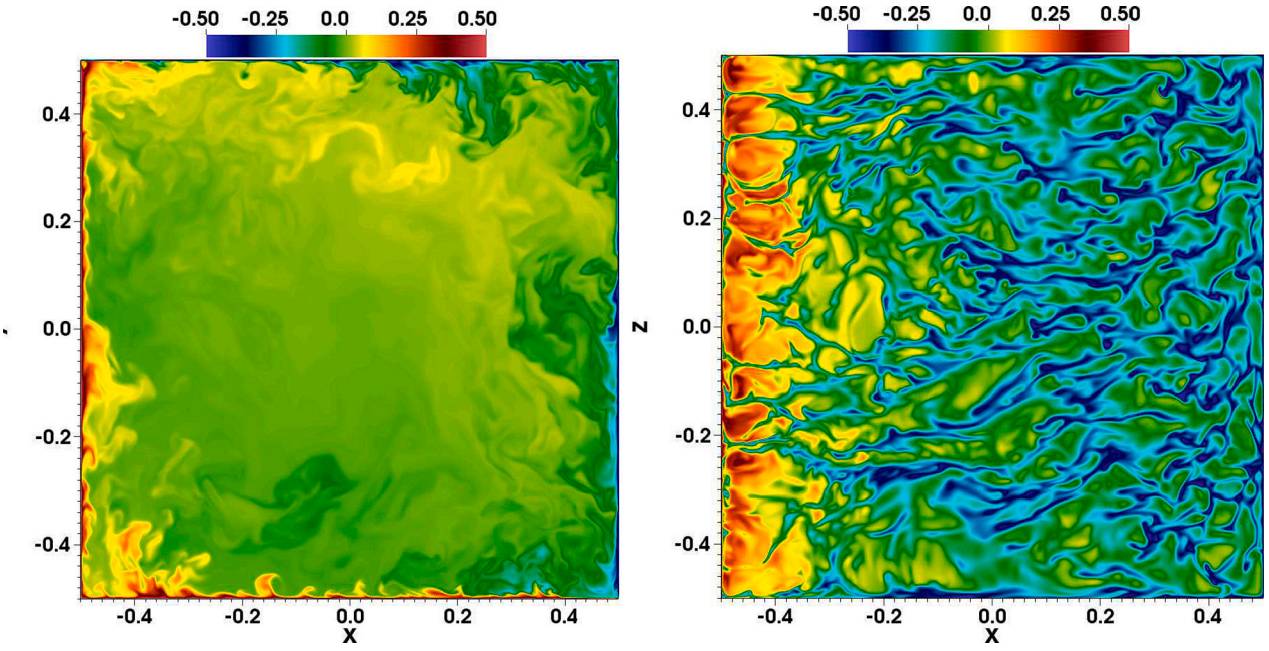

Fig. 4. Instantaneous non-dimensional temperature contours. Left: slice of the cross-section of the room at $z = 0$. Right: slice at $y = 0.495$ near the cold top horizontal wall.

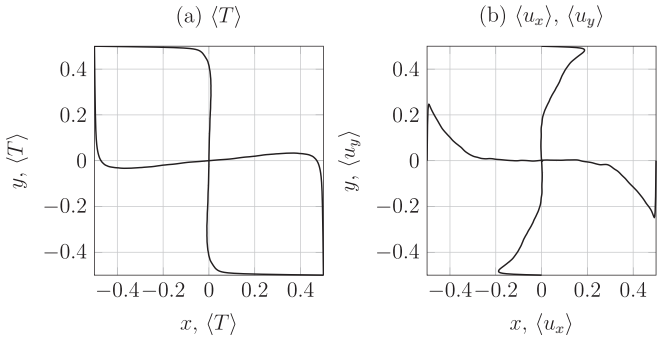

Fig. 5. Time-averaged non-dimensional temperature (a) and velocity (b) profiles along the horizontal and vertical bisectors of the symmetry plane of the cavity z = 0 for $Ra = 3.6 \times 10^9$.

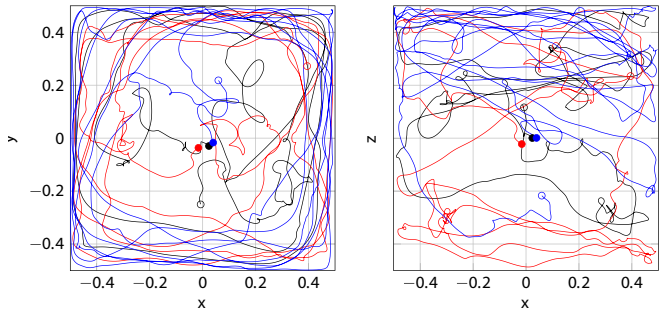

Fig. 6. Three arbitrary particle trajectories (in different color) as seen from the *x*-*y* (left panel) and *x*-*z* (right panel) directions. Filled and empty markers indicate initial and terminal positions for each particle trajectory, respectively.

symmetry plane of the cavity. The maximum vertical and horizontal average velocities are 0.246 and 0.188 in non-dimensional units respectively. Overall mean velocity in the cavity is 0.05.

In dimensional units the maximum average velocity is 0.105 m s^{-1} within the momentum boundary layer and near-zero velocities at the center of the room. Overall, the mean air velocity in the room is 0.021 m s^{-1}, for a Prandtl and Rayleigh number considered.

As an example, Fig. 6 shows $(x - y)$ and $(x - z)$ projections of particle trajectories of three arbitrarily selected particles on the left and right panels, respectively. Filled and empty markers indicate starting and final positions for all three trajectories respectively. Released near the cavity center at $(0, 0, 0)$, particles initially spend some time in this low speed region before being captured and transported by the high-velocity clockwise dominant circulation. The lateral displacement in z direction of the particle trajectories are shown in the vertical projection in the right panel of Fig. 6. The results suggest that the particles do not have any attracting manifolds, nor any preferential location and are circulated across the entire width of the cavity under the action of the dominant large-scale circulation flow.

To study the ability of the background air currents to disperse aerosol clouds we computed the time evolution of the relative dispersion

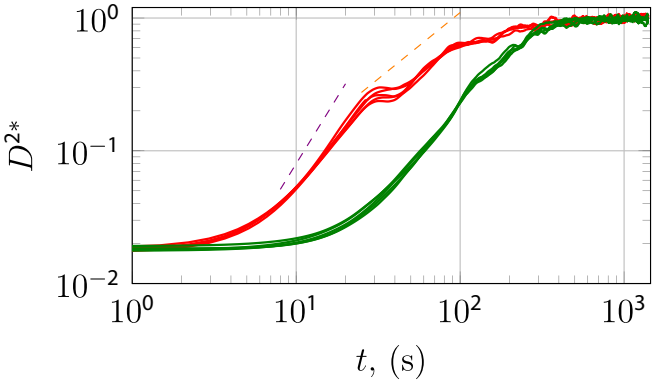

Fig. 7. Temporal evolution of the non-dimensional relative dispersion D^{2*} of particle spheres located in the center (green) and the corner (red) of the cavity for each considered particle size. Violet and orange dashed lines corresponds to shear/ballistic ($\nu = 2$) and linear diffusion ($\nu = 1$) regimes, respectively. (For interpretation of the references to color in this figure legend, the reader is referred to the web version of this article.)

defined in Eq. (14). Fig. 7 shows the temporal evolution of non-dimensional relative dispersion (D^{2*}) for each particle size for the particle clouds located in the corner (red color) and in the center (green color) of the room (see Table 1 for coordinates). We use a uniform color to depict all particle sizes as there is minimal variation in the relative dispersion between the particle sizes for single cloud location. Also, in the case of the red cloud during the plateau period from 20 to 50 s, there are no distinctive trends and regular patterns observed at that moment. The figure shows that clouds of particles with different sizes located in the center of the cavity (green) require more time to initiate dispersion, and that the dispersion rate starts to increase rapidly at around 20 s, whereas the relative dispersion of the particle clouds initially located in the corner (red) start to grow at 3 s. After these initial growths the rate of dispersion in both cases is similar and is maximum with the rate of the ballistic regime. Violet and red dashed lines show shear/ballistic ($\nu = 2$) and linear diffusion ($\nu = 1$) regimes respectively. The average distance between particle pairs continues to grow until 500 s for both cases, where the relative dispersion reaches a plateau with the average distance between particle pairs of $D \sim 2.2$ m. At this point, it stops growing indicating that all particles are homogeneously mixed within the cavity. Aerosol clouds located in the corner reach the highest rate of dispersion at ~15 s, while clouds in the center at ~40 s. In both cases highest dispersion rate is close to ballistic regime.

Fig. 8 shows the non-dimensional temporal evolution of particle size-averaged relative dispersion (D^{2*}_{sa}) of each cloud initially located along the main diagonal of the cavity. Due to near zero average velocities in the center of the cavity the green cloud initially located at the center takes longer to initiate dispersion, reaching the highest rate of dispersion around 40 s after the release. Clouds located close to the center of the main diagonal exhibit asymmetric behavior. During the initial 10 s, the cyan cloud exhibits the highest rate of relative dispersion, surpassing the dispersion rates of the rest of the clouds. While the yellow cloud dispersion surpasses only the green cloud dispersion rate. This indicates the presence of inhomogeneities in the recirculating flow pattern. Both clouds, yellow and cyan, which initially were located to the left and right from the green cloud, reach dispersion rate close to the ballistic regime at ~25 s. The rate of particle relative dispersion of the cyan cloud is similar to the clouds located in the corners of the cavity (red and blue). Both clouds initially located in the opposite corners of the room exhibit similar pattern, with rapid growth of relative dispersion starting from 3 s. These clouds show a plateau between 25 and 60 s. This phenomenon is observed for the clouds seeded near the corners of the cavity. Initially these clouds are advected horizontally along the walls following the large-scale recirculation while the mean separation distance of the particle increases. Eventually though this patch of particles arrive near the vertical wall where the cloud is temporarily shrinks in the direction perpendicular to the vertical wall and resulting in this short term plateau in D^{2*}. As they move vertically turbulent dispersion continues to separate the particle pairs. This distinct feature is not observed in the clouds initially seeded near the center of the cavity that follow a continuously increasing trend of D^{2*}. The cyan sphere does not exhibit this pattern, showing continuous growth. Because of this, the first particle cloud to reach the uniform distribution is cyan, it takes 300 s, while the red, blue and green clouds require 200 s more. All the clouds disperse at a rate between the shear/ballistic and linear regimes, and at a certain point in time, they reach a transition point where the diffusion rate reaches its maximum and subsequently slows down.

The temporal evolution of the size and the location-averaged particle relative dispersion (D^{2*}_{sala}) shown with black thick dashed line in Fig. 8 (subscript *sala* stands for size and location averaged value). The plot can be divided into three distinct stages. The first stage, which spans the initial 10 s, is characterized by the capturing of particles by the flow. In the second stage, there is a rapid growth in the distance between the particles in the clouds, reaching the maximum dispersion rate at 30 s. The third stage commences after the transition point, dispersion rate is following the linear regime ($\nu = 1$), and gradually slows down, until the particles achieve a homogeneous distribution within the room at 500 s.

We computed the size-averaged particle relative diffusivity ($K_{sa}(t)$) using time evolution of the size-averaged particle relative dispersion ($D^2_{sa}(t)$) and Eq. (15). Fig. 9 shows relative diffusivity (K_{sa}) of each cloud, which initial positions with colors defined in Table 1. Additionally, Table 1 shows time and size averaged dispersion coefficient $\langle K_{sa} \rangle$ of each sphere and the average dispersion coefficient averaged over all sphere locations and particle sizes in the last row of the table. Subscript *sa* stands for size averaged value. The black thick dashed line corresponds to the size and location averaged particle relative diffusivity (K_{sala}). The red, blue, and cyan clouds reach their maximum diffusion rates within the time interval of approximately 20 to 40 s. However, due to the effect the cavity walls, the relative diffusivities of the red and blue clouds experience a rapid decline, exhibiting a local minimum, and then subsequently increases again, displaying a local maximum at 50 s for the red cloud and 100 s for the blue cloud. Nature of this phenomenon were already explained (See Fig. 8). In contrast, the remaining particle clouds (cyan, yellow, and green) exhibit continuous growth in their relative diffusivity until they reach their respective maximum rates at 30, 70, and 100 s. After reaching their maximum values, the relative diffusivity of these clouds starts to decline. From 500 s onwards, the rate of relative

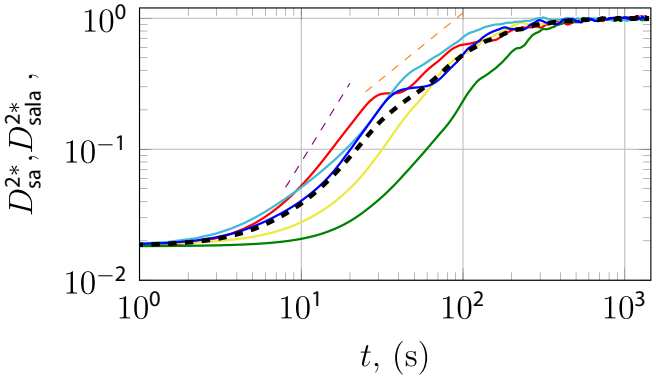

Fig. 8. Temporal evolution of the non-dimensional relative dispersion D^{2*}_{sa} averaged over all particle sizes for each initial position, for color definition see Table 1. Black thick dashed line shows relative dispersion averaged over all particle initial cloud positions and sizes D^{2*}_{sala}. Violet and orange dashed lines corresponds to shear/ballistic ($\nu = 2$) and linear diffusion ($\nu = 1$) regimes respectively. (For interpretation of the references to color in this figure legend, the reader is referred to the web version of this article.)

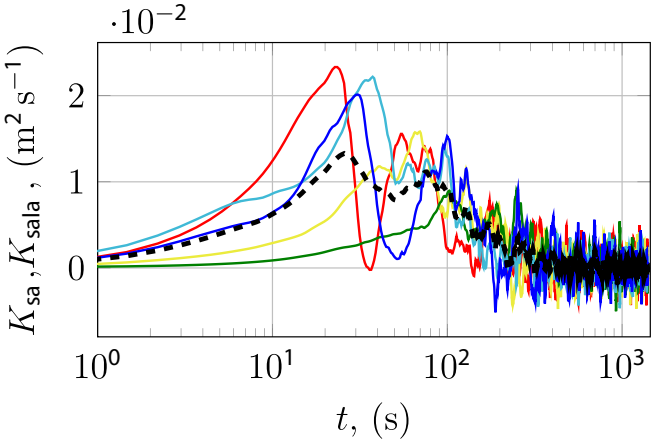

Fig. 9. Temporal evolution of the relative diffusivity K_{sa} in $m^2\ s^{-1}$ averaged over particle sizes for each position, for color definition see Table 1 and averaged temporal evolution of the relative diffusivity K_{sala} in $m^2\ s^{-1}$ averaged over particle sizes and positions is plotted using thick black dashed line.

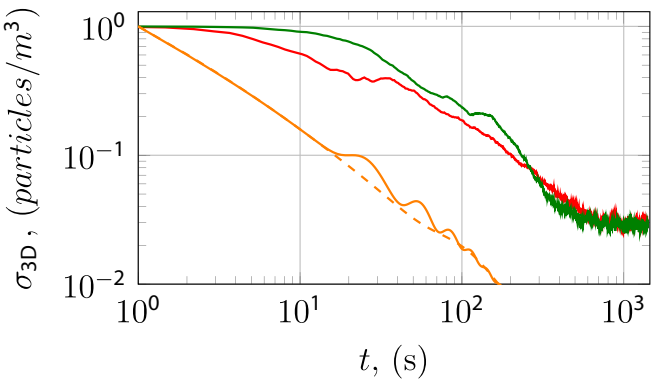

Fig. 10. Temporal evolution of the three-dimensional variance of particle concentration (σ_{3D}) averaged over all particle sizes. DNS results are plotted with red for the cloud located at [−0.4, −0.4, −0.4] and in green for the cloud located at [−0.0, −0.0, −0.0], model results are shown with orange color for the cloud in the corner with the coordinates [−0.4, −0.4, −0.4], dashed line corresponds to $u_c = 0.021$ m s^{-1} and solid line to $u_c = 0.105$ m s^{-1}. (For interpretation of the references to color in this figure legend, the reader is referred to the web version of this article.)

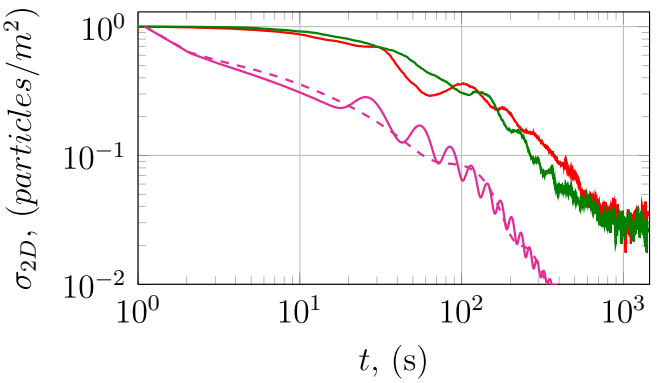

Fig. 11. Temporal evolution of the two-dimensional variance of particle concentration (σ_{2D}) averaged over all particle sizes. DNS results are plotted with red for the cloud located at [−0.4, −0.4, −0.4] and with green for the cloud located at [−0.0, −0.0, −0.0], model results shown with magenta color for the cloud initially located in the corner with coordinates [−0.4, −0.4, −0.4], solid line corresponds to $u_c = 0.105$ and dashed line $u_c = 0.021$. (For interpretation of the references to color in this figure legend, the reader is referred to the web version of this article.)

dispersion fluctuates around zero. The time-averaged dispersion coefficient for each sphere is provided in Table 1.

The averaged temporal evolution of the relative diffusivity averaged over particle sizes shown in Fig. 9 exhibits a rapid increase in relative diffusivity immediately after the release of particles, peaking at approximately 25 s with value of $K_{sala} = 0.013$ m^2 s^{-1}. Subsequently, it decreases and reaches a local minimum at around 50 s, followed by another growth phase up to approximately 70 s, where it reaches a local maximum. However, after reaching the local maximum, the relative diffusivity experiences a rapid decline, exhibiting fluctuations. Around 500 s, the relative diffusivity reaches a statistically stable state, fluctuating around zero.

To compare the dispersion predicted by the DNS with that of the analytical models, we use the variance of the particle concentration as a measure of the dispersion process. To facilitate a comparison the cavity is divided into $5^3 = 125$ equal square bins. We track particle count in each bin, then, by utilizing Eq. (16), we compute the variance of particle concentration, and the results are shown in Fig. 10. On the other hand, Fig. 11 shows the 2D variance of particle concentration, obtained from Lau et al. [35] model, where dispersion is considered only in two dimensions. To compare the results with the DNS, in this case the cavity is divided into $5^2 = 25$ equal rectangular bins from the top-down (x-z) plane, and the particle count in each bin is tracked over time.

Fig. 10 shows the temporal evolution of the three-dimensional variance of particle concentration(σ_{3D}) of the DNS for a cloud located in the corner (red) and the center (green) averaged over all particle sizes. The predictions of the analytical models for the sphere initially located in the bottom left corner (see red sphere in Fig. 2) are plotted with orange color. The solid orange line represents the model results with a velocity (u_c) of 0.105 m s^{-1} which is close to maximum time-averaged velocity in the cavity, while the dashed orange line represents the results with a (u_c) of 0.021 m s^{-1} which corresponds to overall mean air velocity in the room. The dispersion rate predicted by the model appears to be unaffected by changes in velocity. According to the model, the particle concentration variance reaches value of $\sigma_{3D} = 10^{-2}$ *particles*/m^3 at $t = 168$ s, while the DNS particle concentration variance reaches value of $\sigma_{3D} = 8.5 \times 10^{-2}$ *particles*/m^3 and stagnates after 500 s.

Fig. 11 shows the time-dependent evolution of the two-dimensional variance of the particle concentration (σ_{2D}) of the DNS results for the corner red particle cloud and the central green particle cloud, averaged over all particle sizes. Results of the analytical model for the cloud in the corner in magenta, similarly to the 3D case described above are also included in this figure. The dashed magenta line represents the analytical model proposed by Lau et al. [35] with $u_c = 0.021$ m s^{-1}, while the solid magenta line corresponds to $u_c = 0.105$ m s^{-1}. According to the Lau et al. [35] model, the particle concentration variance is $\sigma_{2D} = 10^{-2}$ *particles*/m^2 at $t = 360$ s, while the DNS results projected along Z predict s time of $t = 800$–900 s to achieve fully mixed conditions.

4. Discussion

The dispersion analysis reveals notable differences between the Lau et al. [35] model and the DNS results. The Lau et al. model takes approximately 360 s to reach a dispersion value of $\sigma_{2D} = 10^{-2}$ *particles*/m^2, whereas the DNS simulation achieves homogeneus particle distribution state around 900 s. On the other hand, the model presented in Eq. (7) achieves a similar dispersion value at around 168 s, while the DNS simulation reaches this state at approximately 500 s.

Comparing the 2D and 3D approaches of the DNS results highlights that achieving a homogeneous distribution occurs faster in the 3D case. This disparity suggests that the dispersion behavior predicted by the 2D approach is inaccurate. The results unequivocally demonstrate the failure of the 2D dispersion model to accurately predict the dispersion process. While both analytical models fall short of providing reliable predictions compared to the DNS, the 3D approach in model Eq. (7) yields better results.

Indeed, the DNS simulation offers more accurate predictions of the particle dispersion process within the room compared to the analytical models. The overprediction of the dispersion rate of the analytical models can be attributed to their simplifications, such as assuming a homogeneous and isotropic environment, a constant dispersion coefficient, and neglecting the impact of turbulent eddies on particle dispersion. By considering these simplifications, the analytical models may fail to capture the intricacies of the actual dispersion process, leading to discrepancies with the DNS results.

Upon investigating the effect of velocity in the Gaussian models, it becomes evident that the dispersion rate remains independent of velocity. This conclusion is supported by analyzing Eqs. 7 and 10, where it is observed that the dispersion rate is solely influenced by the dispersion coefficient, while the velocity merely determines the spatial location of the aerosol cloud.

From Fig. 8 and Table 1, it can be observed that the cyan particle

cloud reaches homogeneous dispersion faster compared to other clouds, while the red corner clouds has the largest dispersion coefficient. There is a inconsistency between the two results due to the calculation of K. In Table 1, the value of K is determined based on the relative diffusivity until the time corresponding to the overall maximum value of temporal diffusivity, which on average occurs at around 25 s after the release of the clouds.

5. Conclusion

To better understand the capacity of confined turbulent flows to disperse and homogenize aerosol patches, like those generated during a person's cough or sneeze, we conducted fully-resolved simulations of spherical particle clouds with different particle sizes in a buoyancy-driven turbulent flow in a cubic cavity. The results indicate that the time required to achieve fully mixed conditions depends on the initial location of the cloud. However, the dispersion rate, as measured by relative dispersion and the predictions of variance of particle concentration, remains consistent across the numerical experiments.

The comparison of the DNS results with simplified analytical models reveals that the latter significantly overpredict the rate of dispersion when compared to the fully-resolved simulations.

Both models fail to accurately replicate DNS results. However, our newly developed model, which adopts a 3D approach that aligns more closely with real-world conditions, indicates that the cloud's variance is expected to converge to values similar to those observed in DNS at approximately 168 s. In contrast, the DNS predicts fully mixed conditions after 500 s. On the other hand, the 2D model proposed by Lau et al. [35] indicates that the aerosol cloud would become evenly dispersed in the room after 360 s. In contrast, in a 2D approach, DNS predicts that particles would take 800–900 s to become evenly dispersed after their release. The discrepancy between the simplified models and the DNS results underscores the need for more sophisticated models that can accurately capture the complex dynamics of aerosol dispersion in confined turbulent flows.

Overall, these results provide insights into the dynamics of particle dispersion in a closed room by the action of buoyancy-driven turbulent flow at $Ra = 3.6 \times 10^9$ and highlight presence of non homogeneous flow with time and space dependent dispersion coefficient. The observed temporal evolution of relative dispersion, relative diffusivity, 3D and 2D variance can be used to validate analytical models and improve our understanding of the physical processes involved in particle cloud dispersion. Our findings underscore the limitations of current analytical models and its inability to give reliable and physical results. Our study emphasizes that despite the simple geometry and mechanism of action, buoyancy-driven flow in the cubical cavity is a complex three-dimensional phenomenon characterized by large-scale recirculation patterns with the presence of local instabilities arising from turbulence. These findings highlight the significance of undertaking additional research in this field and the necessity of developing novel, efficient and computationally cheap methods for modeling these processes.

The idealized setup considered in this work does not include additional heat sources nor obstacles representing human presence in the room. Therefore, the dispersion rate and the time to reach fully mixed conditions can be considered as a lower and upper limits, respectively.

CRediT authorship contribution statement

Akim Lavrinenko: Conceptualization, Data curation, Formal analysis, Investigation, Methodology, Software, Validation, Visualization, Writing – original draft, Writing – review & editing. **Alexandre Fabregat:** Conceptualization, Data curation, Formal analysis, Funding acquisition, Investigation, Methodology, Project administration, Resources, Software, Supervision, Validation, Visualization, Writing – original draft, Writing – review & editing. **Fernando Gisbert:** Software. **Jordi Pallares:** Conceptualization, Data curation, Formal analysis, Funding acquisition, Investigation, Methodology, Project administration, Resources, Software, Supervision, Validation, Visualization, Writing – original draft, Writing – review & editing.

Declaration of competing interest

The authors declare the following financial interests/personal relationships which may be considered as potential competing interests:

Akim Lavrinenko, Jordi Pallares, Alexandre Fabregat, Fernando Gisbert reports financial support was provided by Government of Catalonia. Akim Lavrinenko, Jordi Pallares, Alexandre Fabregat, Fernando Gisbert reports financial support was provided by Spain Ministry of Science and Innovation.

Data availability

Data will be made available on request.

Acknowledgments

We would like to extend our sincere appreciation to Andrew Poje for his valuable insights and comments, which have greatly enriched the quality of this manuscript.

This study was funded by the Spanish Ministerio de Ciencia e Innovacion through the grants PID2020-113303GB-C21 and RTI2018-100907-A-I00 (MCIU/AEI/FEDER) and by the Generalitat de Catalunya through the grant 2021 SGR 00732.

Appendix A

The particle transport model, described by Eqs. (4)–(5), incorporates five distinct forces acting on the particles: hydrodynamic drag, lift, buoyancy, thermophoresis, and Brownian motion. In this study, the one-way coupling approach is utilized, assuming that the dispersed phase exerts no influence on the momentum conservation of the carrier phase. This assumption remains valid when dealing with small particles and dilute systems, where the contributions of the dispersed phase to the carrier phase's momentum conservation can be considered negligible

A.1. Drag

Hydrodynamic drag accounts for the fluid resistance or friction a particle experiences as it moves with respect to the carrier phase. The hydrodynamic drag can be characterized by the particle Stokes number defined as the ratio of the particle and flow characteristic times. Small St_p are associated to particles that rapidly react to changes in accelerations in the underlying flow while large Stokes are found in inertia-dominated particles. The Stokes number for a particle of diameter $\widetilde{d}_p$ can be written as:

$$St_p = \frac{d_p^2}{18C_c}\frac{\rho_p}{\mu_f}u_s l_s \tag{18}$$

where ρ_p is the particle density, C_c is the Cunningham correction factor

$$Kn = \frac{2\lambda}{\widetilde{d}_p} \tag{19}$$

$$C_c = 1 + Kn\left[1.205e^{-0.0026/Kn} + 0.425e^{-0.7400/Kn}\right] \tag{20}$$

where $d_p = \widetilde{d}_p/l_s$ is the non-dimensional particle diameter and $\lambda = 6.8 \times 10^{-8}$ m is the free mean path in air at T_0 [50].

A.2. Buoyancy (weight)

The magnitude of the buoyancy force experienced by a particle within a fluid with different density under a gravitational field with acceleration magnitude $g = 9.81\ \mathrm{m\,s^{-2}}$ can be written as:

$$n_g = -g\left(1 - \frac{\rho_f}{\rho_p}\right)\frac{l_s}{u_s^2}. \tag{21}$$

A.3. Thermophoresis

Thermophoresis is the force due to gradients in the temperature field across the particle characteristic length. The pre-factor of the non-dimensional temperature gradient, n_{th}, is defined as [51]:

$$n_{th} = -18\frac{K_{tp}}{d_p^2}\frac{\nu_f^2}{\widetilde{T}_0}\frac{\rho_f}{\rho_p}\frac{T_s}{l_s^2 u_s^2} \tag{22}$$

where the factor K_{tp}, defined as,

$$K_{tp} = \frac{2C_s\left(k_f + 2k_p Kn\right)\left[1 + 2Kn(1.2 + 0.41exp(-0.44/Kn))\right]}{(1 + 6C_m Kn)\left(2k_f + k_p + 4k_p C_t Kn\right)}, \tag{23}$$

contains three constant set to $C_s = 1.17$, $C_m = 1.14$ and $C_t = 2.18$. Note that the negative sign in n_{th} indicates that the force points in the direction of maximal temperature decay.

A.4. Lift

The hydrodynamic force acts perpendicular to the flow direction and is proportional to the cross product of the velocity difference between the two phases and the local vorticity in the carrier phase. The proportionality factor has the form

$$n_l = C_L\frac{\rho_f}{\rho_p} \tag{24}$$

where the lift coefficient C_L is defined as [52]:

$$C_L = \left[5.816\sqrt{\frac{Sr_p}{2Re_p}} - 0.875\frac{Sr_p}{2}\right]\frac{3}{4Sr_p}\frac{J(\varepsilon)}{2.255} \tag{25}$$

where the particle Reynolds number is Re_p, particle Strouhal number is Sr_p, ε and J are determined using the relations:

$$Re_p = \left|u_i^* - u_i\right| d_p Re, \tag{26}$$

$$Sr_p = \frac{\left|\epsilon_{ijk}\left[u_j^* - u_j\right]\omega_k\right|}{\left|u_j^* - u_j\right|^2} d_p, \tag{27}$$

$$\varepsilon = \sqrt{\frac{Sr_p}{Re_p}}, \tag{28}$$

$$J(\varepsilon) = 0.6765\{1 + tanh[2.5log_{10}(\varepsilon + 0.191)]\}\{0.677 + tanh[6(\varepsilon - 0.32)]\}. \tag{29}$$

A.5. Brownian

For small enough particles, the net force due to molecular vibrations may not be negligible and, therefore, contribute to the transport. This Browninan force takes the form [53]:

$$n_i(t) = Z_i\sqrt{\frac{2\pi}{\Delta t}216\frac{\rho_f}{\rho_p^2}\frac{k_B\widetilde{T}_0\nu_f}{d_p^5\pi^2C_c}\frac{\widetilde{i}^3}{\widetilde{l}^i}} \tag{30}$$

where Z_i is independent zero-mean Gaussian random number, $k_B = 1.38064852 \times 10^{-23}$ J K^{-1} is the Boltzmann constant.

A.6. Settling velocity

To gain insight into the role played by the flow hydrodinamics on the wall deposition, the deposition rate is often compared with the settling velocity, v_s. This quantity is determined by assuming that the only forces acting on a particle suspended in a quiescent fluid are drag and buoyancy. Simplifying Eqs. (5), the expression for v_s yields

$$v_s = St_p n_g \delta_{i2}. \tag{31}$$

A.7. Exponential-Lagrangian tracking schemes

Eqs. (4) and (5) are temporally integrated using Exponential-Lagrangian Tracking Schemes (ELTS) [54]. ELTS are inherently stable and offer, at least, $\mathscr{O}(\Delta t^2)$ local truncation errors depending on the application. Details on the ELTS temporal discretization can be found in [44].

Appendix B

In this section, we reproduce derivation of the model proposed by Lau et al. [35] and discuss the key assumptions. Authors have developed a quasi-three-dimensional spatio-temporal model that is quick to run and predicts the concentration of viral aerosols indoors with semi-analytic solution. The model considers an infectious person speaking or breathing and assumes the presence of an air-conditioning unit in the room, driving a recirculating flow, see Fig. 12a

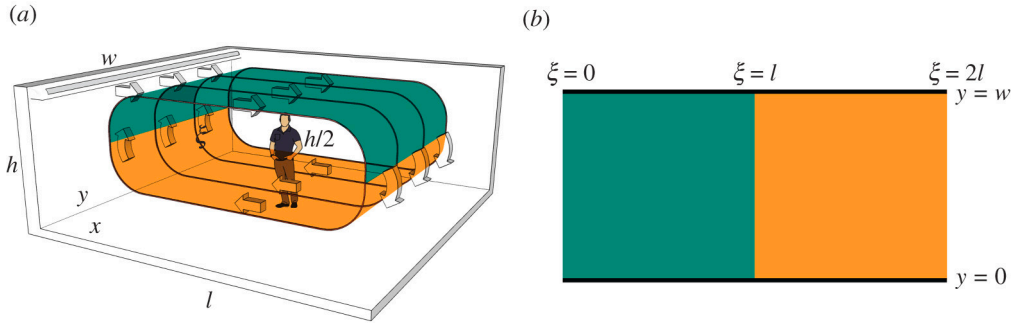

Fig. 12. Sketch of the computational domain. Figure is taken from the paper by Lau Zechariah, Griffiths Ian M., English Aaron and Kaouri Katerina 2022 Predicting the spatio-temporal infection risk in indoor spaces using an efficient airborne transmission modelProc. R. Soc. A.4782021038320210383 https://doi.org/10.1098/rspa.2021.0383, Fig. 2.

The infectious person acts as a continuous source of infectious aerosols, S_{inf}, all aerosols are of the same size and carry the same amount of virus. The aerosols are transported by advection caused by the airflow, which follows the recirculating loop and has velocity u. The aerosols are passively released into the flow stream, so that the advection velocity of the aerosols is also u. The infectious aerosols are assumed to be removed due to three factors: ventilation, biological deactivation of the virus, and gravitational settling. These correspond to sink terms, which are denoted by S_{vent}, S_{deact}, and S_{set}, respectively.

Finally, it assumes turbulent mixing of the air. Turbulence leads to the aerosols diffusing much more rapidly than due to Brownian motion. Turbulent diffusion is governed by the eddy diffusion coefficient, K (m^2/s). From these assumptions, we arrive at the advection-diffusion-reaction (ADR) equation, the governing equation for the concentration of infectious aerosols:

$$\frac{\partial C}{\partial t} + \nabla\cdot(uC) - \nabla\cdot(K\nabla C) = S_{inf} - S_{vent} - S_{deact} - S_{set} \tag{32}$$

Thus, an infectious person talking or breathing at position (ξ_0, y_0) is modelled as follows:

$$S_{inf} = R\delta(\xi - \xi_0)\delta(y - y_0) \tag{33}$$

where $\delta(x)$ is the Dirac delta function.

Furthermore, it is assumed that there is mechanical ventilation provided by air-conditioning units which models the ventilation effect as a sink term of uniform strength over the domain S_{vent}. The biological deactivation and gravitational settling are S_{deact} and S_{set} respectively. In our case we consider that there are no air exchange, viral deactivation and settling in the room thus this terms are 0.

The typical airflow from an air-conditioning unit, $u = 0.1 - 1$ m/s, so it is assumed that the air is an incompressible fluid; that is:

$$\nabla\cdot\mathbf{u} = 0 \tag{34}$$

For a room with length l and width w, the loop surface of the airflow is unwrapped to the two-dimensional domain $(\xi, y) \in [0, 2l] \times [0, w]$, see Fig. 12b. This extended domain allows to model the evolution of the aerosol cloud in both the upper and lower layers of the flow stream in a simpler way. Assuming there is only one infectious person, eqs. 32 is substituted into ADR Eq. (32) to obtain the partial differential equation (PDE), which we will be solving:

$$\frac{\partial C}{\partial t}+u\frac{\partial C}{\partial \xi}-K\left(\frac{\partial^2 C}{\partial \xi^2}+\frac{\partial^2 C}{\partial y^2}\right)=R\delta(\xi-\xi_0)\delta(y-y_0) \tag{35}$$

where **u** is the airflow velocity vector, K is the diffusion coefficient.

In the beginning there are no virus-carrying aerosols, hence, the initial condition is:

$$C(\xi,y,0)=0 \tag{36}$$

In the set-up the aerosols loop around the room. This is modelled through periodic boundary conditions on the concentration and its derivative at the wall $\xi=0$ and the opposite side of the extended domain, at $\xi=2l$. Hence:

$$C(0,y,t)=C(2l,y,t), \tag{37}$$

$$\frac{\partial C}{\partial \xi}(0,y,t)=\frac{\partial C}{\partial \xi}(2l,y,t) \tag{38}$$

The system is closed by applying Neumann boundary conditions at the walls located at $y=0,w$ as follows:

$$\frac{\partial C}{\partial y}(\xi,0,t)=\frac{\partial C}{\partial y}(\xi,w,t)=0 \tag{39}$$

The conditions in Eq. (39) correspond to perfect reflection of aerosols at the wall.

The PDE shown in Eq. (35) is solved with the boundary conditions in Eq. (39) and initial condition in Eq. (36) by first solving the homogeneous problem to determine the impulse function. Then, the impulse is convolved with the source function Eq. (33). Owing to the periodic and Neumann boundary conditions Eq. (39), method of images could be used when solving for the impulse function. Hence, the solution is given by:

$$\begin{aligned}\mathscr{C}(\eta,y,t)=&\int_0^t\frac{R}{4\pi Kt}\sum_{m=-\infty}^{\infty}e^{-\frac{(\eta-ut-\eta_0-2ml)^2}{4Kt}}\times\\&\times\sum_{n=-\infty}^{\infty}\left(e^{-\frac{(y-y_0-2nw)^2}{4Kt}}+e^{-\frac{(y+y_0-2nw)^2}{4Kt}}\right)dt\end{aligned} \tag{40}$$

By leveraging the mapping of the quasi-three-dimensional setup to a two-dimensional geometry, the aerosol concentration is averaged in the upper and lower branches of the loop surface to determine the concentration for the quasi-three-dimensional setup. Specifically, it is defined that $x\in[0,l]$ to be the Cartesian coordinate in the direction of the upper flow, so $x=\eta, 0\le\eta\le l$ defines the upper branch, and $x=2l-\eta$ defines the lower branch for $l\le\eta\le 2l$. The concentration of viral aerosols in the upper branch is then given by:

$$C_{\text{upper}}(x,y,t)=\mathscr{C}(x,y,t) \tag{41}$$

and the concentration of viral aerosols in the lower branch is given by:

$$C_{\text{lower}}(x,y,t)=\mathscr{C}(2l-x,y,t) \tag{42}$$

The separation between the two branches is half the height of the room. It is assumed that within the two branches, the air is well mixed and it is used to transform the two-dimensional expressions back into a three-dimensional representation:

$$C(x,y,t)=\frac{C_{\text{upper}}(x,y,t)+C_{\text{lower}}(x,y,t)}{2}\cdot\frac{h}{2} \tag{43}$$

Then substitute Eq. (40) into Eq. (43) to obtain the total concentration:

$$\begin{aligned}C(x,y,t)=&\frac{2R}{4\pi Kh}\int_0^t\sum_{m=-\infty}^{\infty}\left[e^{-\frac{(x-ut-x_0-2ml)^2}{4Kt}}+e^{-\frac{(x+ut+x_0-2ml)^2}{4Kt}}\right]\times\\&\times\sum_{n=-\infty}^{\infty}\left[e^{-\frac{(y-y_0-2nw)^2}{4Kt}}+e^{-\frac{(y+y_0-2nw)^2}{4Kt}}\right]\end{aligned} \tag{44}$$

References

[1] Khaled Al-Farhany, Mohamed F. Al-dawody, Dhafer A. Hamzah, Wael Al-Kouz, Zafar Said, Numerical investigation of natural convection on Al_2O_3–water porous enclosure partially heated with two fins attached to its hot wall: under the MHD effects, Appl. Nanosci. (2021), https://doi.org/10.1007/s13204-021-01855-y.

[2] S. Shahzad, M. Sheikholeslami, T. Ambreen, A. Shafee, H. Babazadeh, M. Ahmad, Heat transfer management of hybrid nanofluid including radiation and magnetic source terms within a porous domain, Appl. Nanosci. 10 (2020), https://doi.org/10.1007/s13204-020-01432-9.

[3] G.C. Morrison, P. Zhao, L. Kasthuri, The spatial distribution of pollutant transport to and from indoor surfaces, Atmos. Environ. 40 (20) (2006) 3677–3685, https://doi.org/10.1016/j.atmosenv.2006.03.015. URL, https://www.sciencedirect.com/science/article/pii/S1352231006002901.

[4] P. James, A. Stohl, C. Forster, S. Eckhardt, P. Seibert, A. Frank, A 15-year climatology of stratosphere–troposphere exchange with a Lagrangian particle dispersion model 2. Mean climate and seasonal variability, J. Geophys. Res.-Atmos. 108 (D12) (2003), https://doi.org/10.1029/2002JD002639.

[5] I. Manisalidis, E. Stavropoulou, A. Stavropoulos, E. Bezirtzoglou, Environmental and health impacts of air pollution: a review, Front. Public Health 8 (2020), https://doi.org/10.3389/fpubh.2020.00014. URL, https://www.frontiersin.org/articles/10.3389/fpubh.2020.00014.

[6] K. Zhang, S. Batterman, Air pollution and health risks due to vehicle traffic, Sci. Total Environ. 450-451 (2013) 307–316, https://doi.org/10.1016/j.scitotenv.2013.01.074. URL, https://www.sciencedirect.com/science/article/pii/S0048969713001290.

[7] J. Meyerjürgens, M. Ricker, V. Schakau, T.H. Badewien, E.V. Stanev, Relative dispersion of surface drifters in the North Sea: the effect of tides on mesoscale diffusivity, J. Geophys. Res. Oceans 125 (8) (2020) e2019JC015925, https://doi.org/10.1029/2019JC015925. URL, https://agupubs.onlinelibrary.wiley.com/doi/abs/10.1029/2019JC015925.

[8] A. Drescher, Computer Tomography and Optical Remote Sensing: Development for the Study of Indoor Air Pollutant Transport and Dispersion, Ph.D. thesis, Lawrence Berkeley National Laboratory, 1995.

[9] M.P. Wan, C.Y.H. Chao, Y.D. Ng, G. N. S. To, W.C. Yu, Dispersion of expiratory droplets in a general hospital ward with ceiling mixing type mechanical ventilation

system, Aerosol Sci. Technol. 41 (3) (2007) 244–258, https://doi.org/10.1080/02786820601146985.
[10] L. Morawska, J.W. Tang, W. Bahnfleth, P.M. Bluyssen, A. Boerstra, G. Buonanno, J. Cao, S. Dancer, A. Floto, F. Franchimon, C. Haworth, J. Hogeling, C. Isaxon, J. L. Jimenez, J. Kurnitski, Y. Li, M. Loomans, G. Marks, L.C. Marr, L. Mazzarella, A. K. Melikov, S. Miller, D.K. Milton, W. Nazaroff, P.V. Nielsen, C. Noakes, J. Peccia, X. Querol, C. Sekhar, O. Seppänen, S. Ichi Tanabe, R. Tellier, K.W. Tham, P. Wargocki, A. Wierzbicka, M. Yao, How can airborne transmission of COVID-19 indoors be minimised? Environ. Int. 142 (2020) 105832 https://doi.org/10.1016/j.envint.2020.105832. URL, https://www.sciencedirect.com/science/article/pii/S0160412020317876.
[11] Airborne and Direct Contact Diseases, URL, https://www.maine.gov/dhhs/mecdc/infectious-disease/epi/airborne/index.shtml#:~:text=Airborne%20diseases%20are%20caused%20by;particles%2C%20respiratory%20and%20water%20droplets.
[12] Coronavirus Disease (COVID-19): How is it Transmitted?, URL, https://www.who.int/news-room/questions-and-answers/item/coronavirus-disease-covid-19-how-is-it-transmitted.
[13] COVID-19 Coronavirus Pandemic, URL, https://www.worldometers.info/coronavirus/.
[14] CDC Public Health Science Agenda for COVID-19, URL, https://www.cdc.gov/coronavirus/2019-ncov/science/science-agenda-covid19.html.
[15] Global research on coronavirus disease (COVID-19), URL, https://www.who.int/emergencies/diseases/novel-coronavirus-2019/global-research-on-novel-coronavirus-2019-ncov.
[16] J. Shirolkar, C. Coimbra, M. Queiroz McQuay, Fundamental aspects of modeling turbulent particle dispersion in dilute flows, Prog. Energy Combust. Sci. 22 (4) (1996) 363–399, https://doi.org/10.1016/S0360-1285(96)00006-8. URL, https://www.sciencedirect.com/science/article/pii/S0360128596000068.
[17] A. Gadgil, C. Lobscheid, M. Abadie, E. Finlayson, Indoor pollutant mixing time in an isothermal closed room: an investigation using cfd, Atmos. Environ. 37 (39) (2003) 5577–5586. Indoor Air Chemistry and Physics: Papers from Indoor Air 2002, https://doi.org/10.1016/j.atmosenv.2003.09.032. URL, https://www.sciencedirect.com/science/article/pii/S135223100300774X.
[18] N. Klepeis, Modeling Human Exposure to Air Pollution, 2006, https://doi.org/10.1201/9781420012637.ch19.
[19] M.Z. Bazant, J.W.M. Bush, A guideline to limit indoor airborne transmission of COVID-19, Proc. Natl. Acad. Sci. 118 (17) (2021) e2018995118, https://doi.org/10.1073/pnas.2018995118.
[20] M. Auvinen, J. Kuula, T. Grönholm, M. Sühring, A. Hellsten, High-resolution large-eddy simulation of indoor turbulence and its effect on airborne transmission of respiratory pathogens—model validation and infection probability analysis, Phys. Fluids 34 (1) (2022) 015124, https://doi.org/10.1063/5.0076495.
[21] J. Szoplik, M. Ciuksza, Mixing time prediction with artificial neural network model, Chem. Eng. Sci. 246 (2021) 116949, https://doi.org/10.1016/j.ces.2021.116949. URL, https://www.sciencedirect.com/science/article/pii/S0009250921005145.
[22] P. Piscitelli, A. Miani, L. Setti, G. De Gennaro, X. Rodo, B. Artinano, E. Vara, L. Rancan, J. Arias, F. Passarini, P. Barbieri, A. Pallavicini, A. Parente, E.C. D'Oro, C. De Maio, F. Saladino, M. Borelli, E. Colicino, L.M.G. Gonçalves, G. Di Tanna, A. Colao, G.S. Leonardi, A. Baccarelli, F. Dominici, J.P. Ioannidis, J.L. Domingo, The role of outdoor and indoor air quality in the spread of sars-cov-2: overview and recommendations by the research group on covid-19 and particulate matter (rescop commission), Environ. Res. 211 (2022) 113038, https://doi.org/10.1016/j.envres.2022.113038. URL, https://www.sciencedirect.com/science/article/pii/S0013935122003656.
[23] W.W. Nazaroff, Indoor aerosol science aspects of sars-cov-2 transmission, Indoor Air 32 (1) (2022) e12970, https://doi.org/10.1111/ina.12970.
[24] A.A. Lima, I.C.M. Nunes, J.L.D.S. Duarte, L. Meili, P.D.C. Nagliate, A.G.C.D. S. Almeida, Characteristics of sars-cov-2 aerosol dispersion in indoor air: scoping review, Res. Soc. Developm. 10 (4) (2021) e44310414300, https://doi.org/10.33448/rsd-v10i4.14300. URL, https://rsdjournal.org/index.php/rsd/article/view/14300.
[25] D. Ciuzas, T. Prasauskas, E. Krugly, R. Sidaraviciute, A. Jurelionis, L. Seduikyte, V. Kauneliene, A. Wierzbicka, D. Martuzevicius, Characterization of indoor aerosol temporal variations for the real-time management of indoor air quality, Atmos. Environ. 118 (2015) 107–117, https://doi.org/10.1016/j.atmosenv.2015.07.044. URL, https://www.sciencedirect.com/science/article/pii/S1352231015302430.
[26] N. Hobeika, C. García-Sánchez, P.M. Bluyssen, Assessing indoor air quality and ventilation to limit aerosol dispersion; Literature review, Buildings 13 (3) (2023), https://doi.org/10.3390/buildings13030742. URL, https://www.mdpi.com/2075-5309/13/3/742.
[27] J. Wei, Y. Li, Airborne spread of infectious agents in the indoor environment, Am. J. Infect. Control 44 (9, Supplement) (2016) S102–S108. Indoor Air as a Vehicle for Human Pathogens, https://doi.org/10.1016/j.ajic.2016.06.003. URL, https://www.sciencedirect.com/science/article/pii/S0196655316305314.
[28] T. Dbouk, D. Drikakis, Natural ventilation and aerosol particles dispersion indoors, Energies 15 (14) (2022), https://doi.org/10.3390/en15145101. URL, https://www.mdpi.com/1996-1073/15/14/5101.
[29] N. Gao, J. Niu, Modeling particle dispersion and deposition in indoor environments, Atmos. Environ. 41 (18) (2007) 3862–3876, https://doi.org/10.1016/j.atmosenv.2007.01.016. URL, https://www.sciencedirect.com/science/article/pii/S135223100700060X.
[30] A. Fabregat, F. Gisbert, A. Vernet, S. Dutta, K. Mittal, J. Pallares, Direct numerical simulation of the turbulent flow generated during a violent expiratory event, Phys. Fluids 33 (2021) 035122, https://doi.org/10.1063/5.0042086.
[31] A. Fabregat, F. Gisbert, A. Vernet, J.A. Ferré, K. Mittal, S. Dutta, J. Pallarès, Direct numerical simulation of turbulent dispersion of evaporative aerosol clouds produced by an intense expiratory event, Phys. Fluids 33 (3) (2021) 033329, https://doi.org/10.1063/5.0045416.
[32] A. Lavrinenko, A. Fabregat, J. Pallares, Comparison between fully resolved and time-averaged simulations of particle cloud dispersion produced by a violent expiratory event, Acta Mech. Sinica 38 (8) (2022), https://doi.org/10.1007/s10409-022-09032-x.
[33] J. Pallares, A. Fabregat, A. Lavrinenko, H.A. Bin Norshamsudin, G. Janiga, D. F. Fletcher, K. Inthavong, M. Zasimova, V. Ris, N. Ivanov, R. Castilla, P.J. Gamez-Montero, G. Raush, H. Calmet, D. Mira, J. Wedel, M. Štrakl, J. Ravnik, D. Fontes, F. J. de Souza, C. Marchioli, S. Cito, Numerical simulations of the flow and aerosol dispersion in a violent expiratory event: Outcomes of the "2022 International Computational Fluid Dynamics Challenge on violent expiratory events", Phys. Fluids 35 (4) (2023) 045106, https://doi.org/10.1063/5.0143795.
[34] A. V. Baughman, A. J. Gadgil, W. W. Nazaroff, Mixing of a point source pollutant by natural convection flow within a room, Indoor Air 4 (2) 114–122. doi: https://doi.org/10.1111/j.1600-0668.1994.t01-2-00006.x.
[35] Z. Lau, I.M. Griffiths, A. English, K. Kaouri, Predicting the spatiotemporal infection risk in indoor spaces using an efficient airborne transmission model, Proc. Royal Soc. A Math. Phys. Eng. Sci. 478 (2259) (2022) 20210383, https://doi.org/10.1098/rspa.2021.0383. URL, https://royalsocietypublishing.org/doi/abs/10.1098/rspa.2021.0383.
[36] A. Lavrinenko, F. Gisbert, J. Pallares, A. Fabregat, Fully-resolved numerical simulations of the turbulent flow and particle deposition in a cubical cavity with two pairs of differentially heated opposed walls at rayleigh number 3.6×10^9, Int. Commun. Heat Mass Transf. 141 (2023) 106564, https://doi.org/10.1016/j.icheatmasstransfer.2022.106564. URL, https://www.sciencedirect.com/science/article/pii/S0735193322006868.
[37] P.F. Fischer, J.W. Lottes, S.G. Kerkemeier, Nek5000, URL, http://nek5000.mcs.anl.gov.
[38] A. Deville, A. Fischer, A. Mund, R. Gartling, High-order methods for incompressible fluid flow, Appl. Mech. Rev. 56 (3) (2003) B43, https://doi.org/10.1115/1.1566402, arXiv:https://asmedigitalcollection.asme.org/appliedmechanicsreviews/article-pdf/56/3/B43/5439822/b34_1.pdf.
[39] K. Mittal, S. Dutta, P. Fischer, Multirate timestepping for the incompressible navier-stokes equations in overlapping grids, J. Comput. Phys. 437 (2021) 110335, https://doi.org/10.1016/j.jcp.2021.110335. URL, https://www.sciencedirect.com/science/article/pii/S0021999121002308.
[40] A. Fabregat Tomàs, A.C. Poje, T.M. Özgökmen, W.K. Dewar, Dynamics of multiphase turbulent plumes with hybrid buoyancy sources in stratified environments, Phys. Fluids 28 (9) (2016) 095109, https://doi.org/10.1063/1.4963313.
[41] E. Merzari, A. Obabko, P. Fischer, Spectral element methods for liquid metal reactors applications, 2017, https://doi.org/10.48550/ARXIV.1711.09307. URL, https://arxiv.org/abs/1711.09307.
[42] R. Vinuesa, P. Negi, M. Atzori, A. Hanifi, D. Henningson, P. Schlatter, Turbulent boundary layers around wing sections up to rec=1,000,000, Int. J. Heat Fluid Flow 72 (2018) 86–99, https://doi.org/10.1016/j.ijheatfluidflow.2018.04.017. URL, https://www.sciencedirect.com/science/article/pii/S0142727X17311426.
[43] J. Scheel, S. Emran, J. Schumacher, Resolving the fine-scale structure in turbulent Rayleigh-Benard convection, New J. Phys. 15 (11) (2013), https://doi.org/10.1088/1367-2630/15/11/113063.
[44] A. Fabregat, J. Pallarès, Heat transfer and boundary layer analyses of laminar and turbulent natural convection in a cubical cavity with differently heated opposed walls, Int. J. Heat Mass Transf. 151 (2020) 119409, https://doi.org/10.1016/j.ijheatmasstransfer.2020.119409. URL, https://www.sciencedirect.com/science/article/pii/S001793101935731X.
[45] J.H. Seinfeld, S.N. Pandis, Atmospheric Chemistry and Physics: From Air Pollution to Climate Change, Wiley, 2016.
[46] P. Drivas, P. Valberg, B. Murphy, R. Wilson, Modeling indoor air exposure from short-term point source releases, Indoor Air 6 (2004) 271–277, https://doi.org/10.1111/j.1600-0668.1996.00006.x.
[47] R. Shnapp, S. Brizzolara, M. Neamtu-Halic, A. Gambino, M. Holzner, Universal alignment in turbulent pair dispersion, Nat. Commun. 14 (2023), https://doi.org/10.1038/s41467-023-39903-6.
[48] B. Shivamoggi, Relative particle dispersion in two-dimensional and quasi-geostrophic turbulence, Phys. A: Stat. Mechan. Appl. 529 (2019) 121546, https://doi.org/10.1016/j.physa.2019.121546. URL, https://www.sciencedirect.com/science/article/pii/S0378437119309100.
[49] Wikipedia Contributors, Variance — Wikipedia, The Free Encyclopedia (Accessed 2023). URL, https://en.wikipedia.org/wiki/Variance, 2023.
[50] M.D. Allen, O.G. Raabe, Slip correction measurements of spherical solid aerosol particles in an improved millikan apparatus, Aerosol Sci. Technol. 4 (3) (1985) 269–286, https://doi.org/10.1080/02786828508959055.
[51] L. Talbot, R.K. Cheng, R.W. Schefer, D.R. Willis, Thermophoresis of particles in a heated boundary layer, J. Fluid Mech. 101 (4) (1980) 737–758, https://doi.org/10.1017/S0022112080001905.
[52] J.B. McLaughlin, Inertial migration of a small sphere in linear shear flows, J. Fluid Mech. 224 (1991) 261–274, https://doi.org/10.1017/S0022112091001751.
[53] H. Ounis, G. Ahmadi, J.B. McLaughlin, Brownian particle deposition in a directly simulated turbulent channel flow, Phys. Fluids A Fluid Dynam. 5 (6) (1993) 1427–1432, https://doi.org/10.1063/1.858578.
[54] I.E. Barton, Exponential-lagrangian tracking schemes applied to stokes law, J. Fluids Eng. 118 (1996) 85–89.